The Importance of Subcellular Structures to the Modeling of Biological Cells in the Context of Computational Bioelectromagnetics Simulations

Kevin Jerbic[1], Jan Taro Svejda[1], Benedikt Sievert[1], Andreas Rennings[1], Jürg Fröhlich[2] and Daniel Erni[1]

[1] General and Theoretical Electrical Engineering (ATE), Faculty of Engineering, University of Duisburg-Essen, and CENIDE – Center for Nanointegration Duisburg-Essen, D-47048 Duisburg, Germany

[2] Fields at Work GmbH, CH-8032 Zürich, Switzerland

Microdosimetry, Effective Material Properties, Bioelectromagnetic Simulations, Eukaryotic Cell Modelling, Endoplasmic Reticulum

Abstract

Numerical investigation of the interaction of electromagnetic fields with eukaryotic cells requires specifically adapted computer models. Virtual microdosimetry, used to investigate exposure, requires volumetric cell models, which are numerically challenging. For this reason, a method is presented here to determine the current and power densities occurring in single cells and their distinct compartments in a spatially accurate manner as a first step towards multicellular models within the microstructure of tissue layers. To achieve this, 3D models of the electromagnetic exposure of generic eukaryotic cells of different shape (i.e. spherical and ellipsoidal) and internal complexity (i.e. different organelles) are performed in a virtual, FEM-based capacitor experiment in the frequency range from 10 Hz to 100 GHz. In this context, the spectral response of the current and power distribution within the cell compartments is investigated and any effects that occur are attributed either to the dispersive material properties of these compartments or to the geometric characteristics of the cell model investigated in each case. In these investigations, the cell is represented as an anisotropic body with an internal distributed membrane system of low conductivity that mimics the endoplasmic reticulum in a simplified manner. This will be used to determine which details of the cell interior need to be modeled, how the electric field and the current density will be distributed in this region, and where the electromagnetic energy is absorbed in the microstructure regarding electromagnetic microdosimetry. Results show that for 5G frequencies, membranes make a significant contribution to the absorption losses.

I. Introduction

As part of the network expansion towards 5G, people may become increasingly exposed to high-frequency electromagnetic (EM) radiation. Due to ambitious infrastructure projects such as Industry 4.0 or the Internet of Things, this technology shift will not be limited primarily to public spaces as in the past, but will also have a massive impact on the workplace or remote areas such as e.g. smart farming in agriculture. The resulting increase in exposure duration and frequency, as anticipated by the International Commission on Non-Ionizing Radiation Protection (ICNIRP) [ICNIRP, 2020], necessitates a more detailed re-evaluation of existing radiation guidelines. This shift to higher frequencies thereby brings into focus the absorption in the outermost millimeters of the body surface, especially in the skin and the eyes, and raises the question of exactly where in a tissue microstructure the energy absorption occurs. Investigating the effects of the interaction between electromagnetic (EM) fields and biological systems down to the (sub)cellular level therefore requires high-resolution microscopic tissue models.

In order to perform microdosimetric studies to predict this effects of interaction and, in particular the EM energy intake into tissues and their underlying cells, accurate cell models are needed. However, the development of such models is challenging because cells are highly complex symbiotic systems consisting of a multitude of organelles stochastically distributed inside them [Kitano, 2002]. For this

reason, the level of detail used in a model is defined by the most relevant structures significantly influencing the field distribution regarding the electromagnetic field quantities of interest.

For instance, the dielectric spectrosopy of living cell suspensions is based on cell models with a relatively low level of detail. Nevertheless, dielectric spectroscopy has been proven to be an adequate tool to characterize various types of cells (and cell states) and to detect malignant degenerations based on their frequency-dependent macroscopic dielectric properties. Such properties can be phenomenologically described using Debye-type dielectric functions [Asami et al., 1979; Asami et al., 1989; Lisin et al., 1996; Polevaya et al., 1999], from which it is possible to infer the properties of individual cell compartments, such as the membrane or the cytoplasm. This is done by a two-step formalism in which mixing formulas are first applied to the whole cell suspension and then, under the basic assumption of a simplified spherical double-shell model, to the eukaryotic cells contained within [Sihvola, 2008; Asami, 2002]. Following this formalism, a cell representation was created that corresponded to the statistical average of all cells contained in the suspension allowing physiological changes to be associated with physical mechanisms [Ermolina et al., 2000; Ermolina et al., 2001; Feldman et al., 2003].

With the development of suitable biosensors, it is now possible to perform spectroscopy on single cells. In addition, improvements in computer hardware and software allow more detailed microdosimetric studies of field-cell interaction involving digital twins of the underlying experiments [Merla et al., 2018; García-Sánchez et al., 2018; Merla et al., 2019; Feng et al., 2019; Guo et al., 2021] and a much higher level of detail in the cell models used. Due to the stochastic nature of cells, which is expressed in their size, shape and internal organization, an adequate morphological and dielectric representation of the cell under investigation is required [Ermolina et al., 2001; Merla et al., 2009; Merla et al., 2012; Denzi et al., 2013; Denzi et al., 2015]. For example, the most accurate cell models currently available are from the field of electroporation. There, cell shape modeling is of particular importance in microdosimetric studies of the induced transmembrane potential and the prediction of the local poration of cell membranes. Thus, fluorescence microscopy is used alongside edge detection and extraction algorithms to incorporate the individual shape of the plasma membrane as well as that of the internal organelles. Two- and three-dimensional models generated in this manner are introduced in [Denzi et al., 2016; Denzi et al., 2017; Denzi et al., 2018; de Angelis et al., 2019] and [Pucihar et al., 2006; Towhidi et al., 2008; de Angelis et al., 2020], respectively. These models represent the cell in the context of the experiment performed and thus consider the cross-section of a cell adhering to a coverslip in corresponding simulations. In contrast to electroporation studies, microdosimetric studies for risk assessment require volumetric representation of eukaryotic cells, which allows spatial resolution of electric fields in a heterogeneous cell interior that is not distorted by unnatural deformations. In other words, the level of detail of cell modeling would need to be augmented toward a fully resolved, three-dimensional representation of the cell interior. Following this essential idea, generic 3D cell models, containing organelles such as the endoplasmic reticulum (ER), were designed to answer the following questions: (1) Which are the relevant details which have to be modelled? (2) How is the electric field or current density distributed in the cell interior? (3) Where is electromagnetic energy absorbed?

Thus, in the present study, generic eukaryotic cells of different shapes and internal complexity are investigated using 3D models based on the finite element method (FEM). The cells under consideration start from a simple spherical cell containing only a nucleus and increase in complexity to an ellipsoidal cell comprising a fully resolved endoplasmic reticulum. Using a virtual capacitor experiment, it is investigated how a cell has to be modeled in order to conduct microdosimetric investigations in the sense of risk assessment [IEEE, 2019; ICNIRP, 2020]. Special attention has been paid to the internal structure of the cell, focusing on its size and shape and that of its organelles, all of which are surrounded by a membrane of low conductivity. Based on this, single cells are considered as distributed membrane systems, which can be used to answer the question of whether it is necessary to consider the membrane in the modeling procedure in the frequency range between 10 Hz and 100 GHz. The microdosimetric investigations conducted here will thus be mainly based on three measures: the anisotropic current and loss distribution within the cell alongside the membrane voltages. In addition, the effects of the cell structure on the effective material parameters of the cells under investigation.

The methodology is introduced and the cell models used are outlined in Sec. II. Then, eukaryotic cell models of different complexity are investigated with respect to their internal current and voltage distribution. The results of these investigations are presented and discussed in Sec. III. A conclusion and outlook are given in Sec. IV followed by an appendix where the mixing rule procedure to verify the results is provided in closer detail.

II. Methodology

The methodology section includes three parts. In the first subsection, the eukaryotic cell models under investigation are introduced alongside a method used to spatially resolve and decompose the cell interior for microdosimetric investigations focusing on current and loss distributions within the cell models. In the next subsection, a simulation setup is presented to perform an FEM-based capacitor experiment to predict the distribution of EM fields within the cell and determine effective macroscopic material properties. In the last subsection, the dispersive material properties of the cell compartments are given in detail.

A. Eukaryotic Cell Models and Spatial Segmentation

The three generic cell models investigated in this study are depicted in Fig.1(a)-(c): (a) a simple spherical cell containing a spherical nucleus, (b) an ellipsoidal cell containing a spherical nucleus and (c) an ellipsoidal cell containing both a spherical nucleus and a distributed endoplasmic reticulum (ER). The so-called rough ER is approximated by cisternae which surround the nucleus concentrically.

Taking this structure into account, the cell interior can be divided into two or three compartments: the cytoplasm (CP), the nucleoplasm (NP), and the endoplasmic reticulum (ER), each separated from the other and from the exterior surrounding, i.e. extracellular medium (EC), by a lipid membrane of low conductivity. The subdivision of the cell interior into separate (computational) domains allows field distributions to be determined with a spatial resolution that allows current and loss densities to be integrated. The volumetric segmentation is shown as an illustrative example for the most complex cell model in Fig.1(d)-(f). In addition, the (cross-)sectional segmentation of the cells is shown in Fig.1(g)-(i) allowing the determination of electromagnetic fields in the XY, YZ, and XZ planes. Using these sectional planes in combination with the volumetric segmentation of the cell into its compartments, it is possible to determine the currents flowing through each of them, as shown in Fig.1(j)-(l).

The simple spherical model shown in Fig.1(a) is based on lymphocytes. Lymphocytes were chosen as a template for an initial cell model for two reasons: (1) Their dielectric properties have been extensively studied by the dielectric spectroscopy community [Ermolina et al., 2001; Feldman et al., 2003]. (2) They have a very uniform round shape and their internal structure is very well documented, allowing the study of membrane properties on a cell geometry of low complexity. According to [Asami et al., 1989], their nucleus occupies about 40 % to 70 % of the cell volume and the cytoplasm surrounding the nucleus is poor in organelles. Due to these physiological properties, this first model is well suited for the verification of bottom-up multiscale modeling using mixing rules [Ermolina et al., 2000]. In this study, however, the spherical cell model is investigated with respect to the size of the nucleus using numerical simulations. The ratio of the volume of the nucleus to that of the whole cell c_N normally ranges from 0.4 to 0.7, but here has been extended to cover 0.3 to 0.9 in order to investigate more extreme cases. Following [Ermolina et al., 2000], the cell radius was chosen to be $r_\mathrm{cell} = 7\,\mu\mathrm{m}$, resulting in minimum and maximum radii of $r_\mathrm{N,min} = 4.69\,\mu\mathrm{m}$ and $r_\mathrm{N,max} = 6.76\,\mu\mathrm{m}$ derived from the range given above using $r_\mathrm{N} = \sqrt[3]{c_\mathrm{N}} \cdot r_\mathrm{cell}$. In addition, the reference nuclear radius is $r_\mathrm{N,ref} = 5.9\,\mu\mathrm{m}$ corresponding to $c_\mathrm{N} = 0.6$.

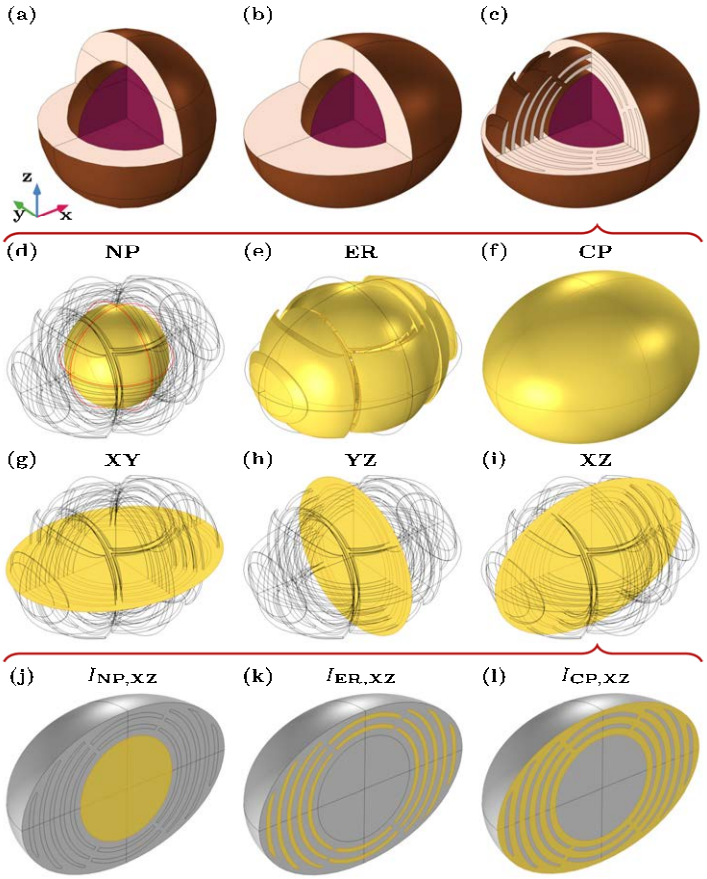

Fig.1: Overview of the cell models studied and the segmentation used for post-processing: (a)-(c) Generic eukaryotic cells of different shapes and internal complexity. Starting with a simple spherical cell model containing only a nucleus (N) in (a), the level of complexity increases to an ellipsoidal cell model comprising a fully resolved endoplasmic reticulum (ER) in (c). (d)-(f) Segmentation of the cell interior into (computational) domains to capture integral quantities such as the corresponding compartment losses. In the given example, the domains highlighted correspond to the nucleoplasm (NP), the endoplasmic reticulum (ER) and the cytoplasm (CP). (g)-(i) Sectional planes for the evaluation and integration of internal fields showing the XY, YZ and XZ planes respectively. (j)-(l) Segmentation of the sectional planes to capture integral quantities such as the corresponding compartment currents. In the given example, the areas correspond to the currents in the nucleoplasm, the endoplasmic reticulum and the cytoplasm in the XZ plane. The areas of the sectional planes corresponding to the integration are highlighted.

In order to investigate the influence of compartmentalization within the cell, the simple spherical cell model is now extended to a more realistic approximation of a cell in the following two steps. Keeping the nuclear radius at a value of $r_{\mathrm{N,ref}} = 5.9\,\mu\mathrm{m}$, which was previously considered as the reference radius, the plasma membrane is first transformed into an ellipsoidal one with semi-axes $s_{\mathrm{x}} = 13\,\mu\mathrm{m}$, $s_{\mathrm{y}} = 10.5\,\mu\mathrm{m}$ and $s_{\mathrm{z}} = 9\,\mu\mathrm{m}$ (cf. Fig.1(b)). The influence of this change of shape on the macroscopic material properties and the microdosimetric measures is investigated with respect to the resulting anisotropy. To capture the microdosimetric current density and loss distribution within the cell in the context of more realistic cell modeling, a distinct ER was added to the cell in a second step, allowing the cell to be studied as a distributed membrane system (cf. Fig.1(c)). The ratio of the volume of the ER to the total cell volume is $c_{\mathrm{ER}} = 0.2$, that of the cytoplasm is $c_{\mathrm{CP}} = 0.63$ and that of the nucleus, $c_{\mathrm{N}} = 0.17$. The thickness of the cell membrane and that of the elements of the ER is $t_{\mathrm{M}} = 7\,\mathrm{nm}$ and that of the nuclear envelope is $t_{\mathrm{NE}} = 40\,\mathrm{nm}$. To provide a better overview, the geometrical properties are summarized in Tab.1.

Tab.1: Geometrical properties of the cell models under investigation. SC, EC and ER denote «spherical cell», «ellipsoidal cell» and «endoplasmic reticulum».

	SC	EC	ER
r_{cell}	7 µm	–	–
s_{x}	–	13 µm	13 µm
s_{y}	–	10.5 µm	10.5 µm
s_{z}	–	9 µm	9 µm
$r_{\mathrm{N,(ref)}}$	(5.9 µm)	5.9 µm	5.9 µm
t_{M}	7 nm	7 nm	7 nm
t_{NE}	40 nm	40 nm	40 nm
$c_{\mathrm{N,(ref)}}$	(0.6)	0.17	0.17
c_{ER}	–	–	0.2
c_{CP}	0.4	0.83	0.63

B. Simulation Setup and Cell Investigations

The three cell models displayed in Fig.1 were placed in a virtual parallel plate capacitor setup to conduct a quasi-static EM analysis between 10 Hz and 100 GHz. This analysis had two goals: (1) The investigation of the influence of internal organelles on the field distribution within a cell (i.e. microdosimetry) and (2) the investigation of this influence on the effective material properties of the simulated suspension. To do this, the capacitor setup was implemented in the finite-element-method-based (FEM) software package *COMSOL Multiphysics* [COMSOL]. A 2D schematic of the 3D setup is given in Fig.2(a). The edge length of the cube-shaped computational domain was 50 µm and was chosen to be large enough to minimize the influence of the depolarization fields around the cells on the neighboring cells. The resulting volume fraction of a cell in the computational domain was 1.15 % for the spherical cell and 4.12 % for the ellipsoidal ones. As depicted in Fig.2(a), a time-harmonic voltage with constant amplitude, $U_0 = \varphi_1 - \varphi_0$, was applied between two opposing outer boundaries of the computational domain that were designed to be electrodes (i.e Dirichlet boundary conditions). The four remaining boundaries were defined with periodic boundary conditions (PBC) in order to suppress fringing fields and to reduce the memory resources of the subsequent quasi-static EM simulation. Due to this setup, the (computational) unit cell is virtually periodically continued in each direction indicated by the PBC. This approach was used in the past to investigate the effective material parameters of randomized (bio-)composites [Jerbic et al., 2020; Krakovsky and Myroshnychenko, 2002], and single cells [Huclova et al., 2010; Froehlich et al., 2014]. A description on how these simulations are verified by mixing rules is given in the Appendix. In order to cope with the anisotropy of the cells under investigation, the voltage U_0 is then applied in the other (orthogonal) directions while swapping the electrodes with the PBCs (and vice versa). This low volume fraction in combination with the setup (i.e., the electrodes and PBCs) allows the interpretation of the cell under investigation either as a representative of a cell suspension corresponding to the static mean [Ermolina et al., 2000], or as a specific single cell [Guo et al., 2021; Chien et al., 2018].

In order to avoid high aspect ratios in the modeling mesh, the plasma membrane and the membranes of the cell organelles are modelled by a set of equations taking into account the conduction and the displacement current

$$\vec{\mathrm{n}} \cdot \vec{\underline{J}}_{\mathrm{up}} = \frac{1}{t_{\mathrm{M}}} \left(\sigma_M + j\omega\varepsilon_0\varepsilon_{\mathrm{r,M}}\right)\left(\underline{\varphi}_{\mathrm{up}} - \underline{\varphi}_{\mathrm{down}}\right) \tag{1}$$

$$\vec{\mathrm{n}} \cdot \vec{\underline{J}}_{\mathrm{down}} = \frac{1}{t_{\mathrm{M}}} \left(\sigma_M + j\omega\varepsilon_0\varepsilon_{\mathrm{r,M}}\right)\left(\underline{\varphi}_{\mathrm{down}} - \underline{\varphi}_{\mathrm{up}}\right) \tag{2}$$

where $\underline{\varphi}_{\mathrm{up/down}}$ and $\vec{\mathrm{n}} \cdot \vec{\underline{J}}_{\mathrm{up/down}}$ denote the membrane potentials and current densities normal to the upper and lower surfaces of the membrane. t_{M} represent the thickness of the membrane while,

σ_M and $\varepsilon_{\mathrm{r,M}}$, represents the conductivity and the relative permittivity of the membrane respectively. ε_0 denotes the vacuum permittivity. Referring to Eqs.(1) and (2), thin membranes can now be represented by these tailored boundary conditions yielding a highly economic treatment as already proposed in [Huclova, 2011].

The simulation was performed on a PC equipped with two Intel Xeon E5-2697 V4 processors (36 cores) and 512 GB of RAM. In this study, a frequency range between 10 Hz and 100 GHz was investigated and sampled with 50 frequency points distributed logarithmically. The data points in between these sampled points were interpolated using piecewise cubic Hermite splines in post-processing. The simulation for each frequency point lasted approximately 30 min using a MUMPS solver. The post-processing of the data was performed within the MATLAB programming environment (version R2020a) [MATLAB].

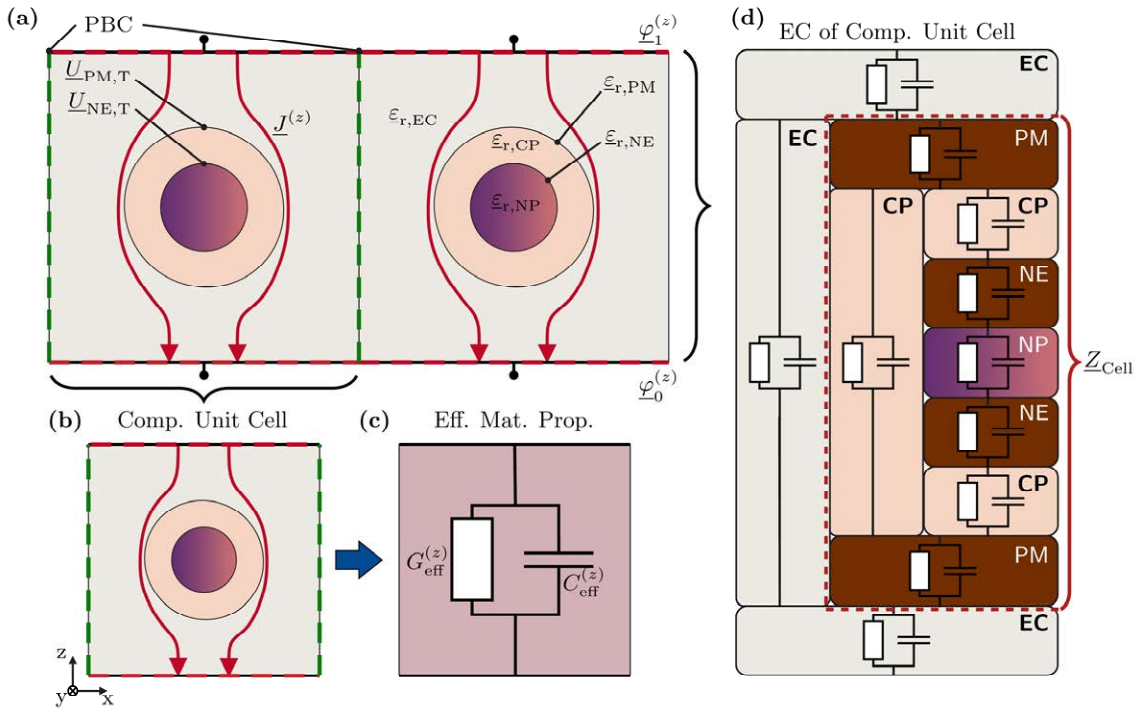

Fig.2: Overview of the virtual capacitor experiment used for the quasi-static EM analysis of the unit cell: (a)-(c) The voltage, $U_0 = \varphi_1 - \varphi_0$, was applied to two opposing sides of the virtual capacitor set up which were considered to obey Dirichlet boundary conditions. Periodic boundary conditions (PBC) were applied to the remaining sides of the computational domain. This set up can be interpreted as a spatially periodic (computational) unit cell. By applying an equivalent circuit-based homogenization, effective material parameters can be calculated, leading to a shunt representation of this unit cell. In addition, the material properties of the individual cell compartments and those of the extracellular medium are assigned dispersive material parameters. To conduct microdosimetry, point evaluations of the transmembrane potential can be determined. (d) Equivalent circuit representation of the biological cell without an endoplasmic reticulum dividing the computational unit cell into several circuit paths. This uses the segmentation depicted in Fig. 1 to determine integral microdosimetric measures such as the losses occurring in or currents flowing through the compartments. These circuit paths are represented by a parallel arrangement of a resistor and a capacitor. The capitals in each circuit path correspond to the individual compartments of the unit cell which are the extracellular medium (EC), and those within the cell, namely, *the plasma membrane (PM), the cytoplasm (CP), the nuclear envelope (NE) and the nucleoplasm (NP). The equivalent circuit depicted in (d), however, was not used for an initial circuit analysis and is only intended to illustrate the order behind the spatial segmentation of the cell and its potential to selectively access arbitrary electrical quantities inside the cell.*

Microdosimetic Investigations

In order to conduct microdosimetric investigations, the potential difference across the plasma membrane and that across the nuclear envelope were monitored (cf. Fig.2(a)). In addition, the currents passing through the cell compartments were observed by integrating the current density normal to the cross-

sectional area of the cell. The losses occurring within the compartments were evaluated by integrating the loss density over their volumes. This was performed by using the segmentation of the cells introduced earlier (cf. Fig.1). In this manner, the spatial observation of microdosimetric quantities, such as the losses occurring in the compartments or the currents flowing through them, enables the interpretation of the biological cells as equivalent circuits, as shown in Fig.2(d) for the example of the simple spherical cell. Following this idea, the segmentation of the cell allows the determination of microdosimetric quantities for the individual compartments of the unit cell, namely the extracellular medium (EC), the plasma membrane (PM), the cytoplasm (CP), the nuclear envelope (NE), and the nucleoplasm (NP). In this simplification, all the possible current paths are summarized by RC shunt impedances. Thus, the cell can be summarized as an overall frequency-dependent impedance, $Z_{\mathrm{cell}}(\omega)$, consisting of frequency-dependent impedances for each organelle. To maintain clarity, the equivalent circuit depicted in Fig.2(d) was not used for an equivalent circuit analysis such as performed in [Merla et al., 2012] and [Denzi et al., 2015]. It is only to illustrate that the spatial segmentation of the cell allows selective access to arbitrary electrical quantities inside the cell.

Effective Material Properties

In addition to these microdosimetric measures, the effective material parameters of the cell (suspension) were determined using this virtual capacitor experiment as depicted in Fig.2 (b) and (c). Time-harmonic quasi-static EM analysis in the form of the capacitor setup presented above leads to an effective admittance that is represented by an equivalent electrical parallel circuit consisting of the elements $G^{\mathrm{eff}}(\omega)$ and $C^{\mathrm{eff}}(\omega)$. This is given by

$$\underline{Y}^{\mathrm{eff}}(\omega) = \frac{\underline{I}(\omega)}{\underline{U}_0} = G^{\mathrm{eff}}(\omega) + j\omega C^{\mathrm{eff}}(\omega) \tag{3}$$

where the applied voltage, $\underline{U}_0$, and the resulting current, $\underline{I}(\omega)$, are directly accessible via COMSOL Multiphysics for an angular frequency $\omega = 2\pi f$. The dispersive effective material properties, ${\varepsilon_r}^{\mathrm{eff}}(\omega)$ and $\sigma^{\mathrm{eff}}(\omega)$, are thus easily deduced according to

$$\underline{Y}^{\mathrm{eff}}(\omega)\frac{d}{A} = \frac{\underline{I}(\omega)}{\underline{U}_0}\frac{d}{A} = \underbrace{\sigma^{\mathrm{eff}}(\omega) + j\omega\varepsilon_0{\varepsilon_r}^{\mathrm{eff}}(\omega)}_{\underline{\sigma}^{\mathrm{eff}}(\omega)} \tag{4}$$

where d is the parallel plate distance and A is the area of the electrode. In Eq. (4), the right-hand term can be interpreted as the complex effective conductivity of the homogenized effective material, $\underline{\sigma}^{\mathrm{eff}}(\omega)$, from which the required material parameters directly follow:

$$\sigma^{\mathrm{eff}}(\omega) = \mathrm{Re}\{\underline{\sigma}^{\mathrm{eff}}(\omega)\} \tag{5}$$

$${\varepsilon_{\mathrm{r}}}^{\mathrm{eff}}(\omega) = \frac{\mathrm{Im}\{\underline{\sigma}^{\mathrm{eff}}(\omega)\}}{\omega\varepsilon_0} \tag{6}$$

In order to consider anisotropies in the effective material, the quasi-static capacitor analysis is performed with excitation in the *x*, *y* and *z* directions yielding corresponding frequency-dependent second-rank tensors for the effective permittivity and effective conductivity,

$$\overleftrightarrow{\sigma}^{\mathrm{eff}}(\omega) = \begin{pmatrix} {\sigma_{\mathrm{x}}}^{\mathrm{eff}}(\omega) & 0 & 0 \\ 0 & {\sigma_{\mathrm{y}}}^{\mathrm{eff}}(\omega) & 0 \\ 0 & 0 & {\sigma_{\mathrm{z}}}^{\mathrm{eff}}(\omega) \end{pmatrix} \tag{7}$$

and for the permittivity,

$$\overleftrightarrow{\varepsilon}_{\mathrm{r}}^{\mathrm{eff}}(\omega) = \begin{pmatrix} {\varepsilon_{\mathrm{r,x}}}^{\mathrm{eff}}(\omega) & 0 & 0 \\ 0 & {\varepsilon_{\mathrm{r,y}}}^{\mathrm{eff}}(\omega) & 0 \\ 0 & 0 & {\varepsilon_{\mathrm{r,z}}}^{\mathrm{eff}}(\omega) \end{pmatrix}. \tag{8}$$

These are the homogenized, frequency-dependent effective material representations.

C. Derivation of the Dispersive Material Properties Based on Published Data

All cell components have dispersive material properties which are modelled using a lossy Debye-type frequency dependence:

$$\underline{\varepsilon}_{\mathrm{r}}(\omega) = \varepsilon_{\mathrm{r},\infty} + \frac{\varepsilon_{\mathrm{r,s}} - \varepsilon_{\infty}}{1 + j\frac{\omega}{\omega_0}} - j\frac{\sigma_{\mathrm{s}}}{\varepsilon_0 \omega} \tag{9}$$

were $\varepsilon_{\mathrm{r},\infty}$ and $\varepsilon_{\mathrm{r,s}}$ denote the permittivity at the high frequency and the low frequency limit of the underlying polarization mechanism respectively. σ_{s} stands for the DC conductivity of the material.

As suggested by [Kotnik and Miklavčič, 2000], [Peyman et al., 2007] and [Merla et al., 2009], the dispersive properties of the extracellular medium, the cytoplasm and the nucleoplasm were approximated using the dielectric functions of physiological salt solutions. To be more precise, they were based on measurements of a phosphate-buffered saline solution (PBS) at 27°C between 100 MHz and 2 GHz performed by [Merla et al., 2009]. Based on an experimental assessment of the cytoplasmic conductivity in [Denz et al., 2015], the conductivity of both the cytoplasm and nucleoplasm was set to 0.32 S/m. Although the membranes of cells and organelles are complex (sub-)structures bound by proteins and filaments of the cytoskeleton, and thus are not a simple phospholipid bilayer (see [Weaver, 2003; Gowrishankar et al., 2006; Gowrishankar and Weaver, 2006), the material parameters of the membrane were assigned values based approximately on measurements of unilaminar liposome vesicles. These measurements were also performed in [Merla et al., 2009]. The material coefficients corresponding to the compartments are summarized in Tab.2 and are in accordance with measurements documented in scientific literature (see [Ermolina et al., 2000]).

Tab.2: Debye coefficients of the underlying materials related to the specific cell compartments.

Compartment	$\boldsymbol{\varepsilon_{\mathrm{r,s}}}$	$\boldsymbol{\varepsilon_{\mathrm{r},\infty}}$	$\boldsymbol{f_0}$ **(GHz)**	$\boldsymbol{\sigma_{\mathrm{s}}}$
Cytoplasm (CP)	67	5	17.9	0.32
Plasma Membrane (PM)	11.7	4	0.18	0.11e-6
Nucleoplasm (NP)	67	5	17.9	0.32
Nuclear Envelope (NE)	11.7	4	0.18	0.11e-6
Extracellular Medium (EC)	67	5	17.9	0.55

The relative permittivity and the conductivity of these compartments are displayed in Fig.3(a) and (b) respectively. The dispersive permittivities of the EC, CP and NP are identical, as are those of the PM and the NE. These spectral responses for the permittivities can be divided into three frequency intervals corresponding to the changes in the dielectric function of the material properties with frequency, i.e. the start and end of the roll-off of the two particular characteristic responses within the investigated range. These intervals are highlighted in shades of blue in Fig.3(a). The conductivity of the compartments can also be divided into three intervals, partially overlapping those of the permittivity, highlighted in shades of red at the top of Fig.3(b). The overlapping ranges of these intervals lead to further segmentation of the investigated spectrum into five frequency ranges highlighted in shades of beige which are enumerated by circled numbers in Fig.3(a).

To provide a better overview, these ranges are summarized in Tab.3. As outlined above, the frequency ranges defined by changes in the dispersive material properties of the cell compartments and the extracellular space will also be plotted in shades of beige above any further graph to show any correspondence to changes in the effective material properties and the microdosimetric measures. These ranges will be referred to as material ranges (MR) 1-5.

Tab.3: Frequency sub-intervals corresponding to changes in the dispersive material parameters of the cell compartments and the extracellular medium displayed in Fig.3 highlighted in shades of beige at the top of the graphs. For further analysis, these sub-intervals will be referred to as "material ranges".

	MR 1	**MR 2**	**MR 3**	**MR 4**	**MR 5**
f	10 Hz to 40 kHz	40 kHz to 30 MHz	30 MHz to 800 MHz	800 MHz to 2 GHz	2 GHz to 100 GHz

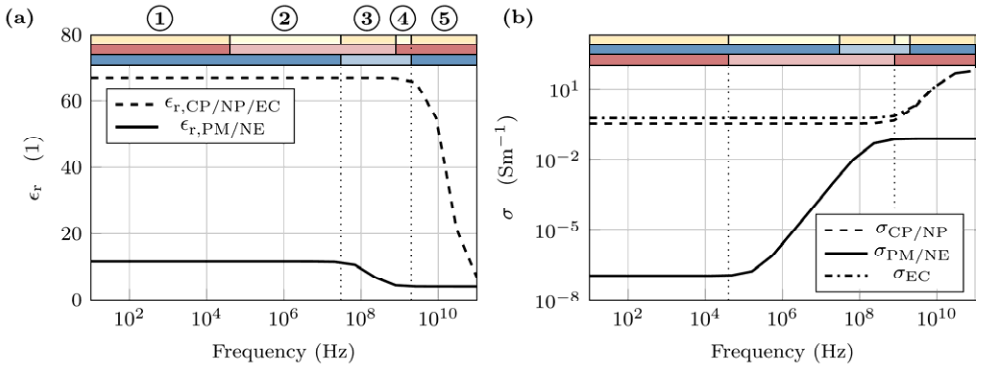

Fig.3: Overview of the dispersive material parameters: In (a), the relative permittivity of the cytoplasm (CP), nucleoplasm (NP) and the extracellular medium (EC) is represented as a dashed line, and that of the plasma membrane (PM) and the nuclear envelope (NE) as a solid line. In (b), the conductivity of the cytoplasm (CP) and nucleoplasm (NP) is represented as a dashed line, that of the plasma membrane (PM) and the nuclear envelope (NE) as a solid line, and that of the extracellular medium (EC) as a dash-dotted line. The bar displayed in shades of blue corresponds to changes in the spectral response of the relative permittivity while the bar displayed in shades of red corresponds to changes in the conductivity. The overlapping ranges of these intervals lead to further segmentation of the investigated spectrum into five frequency ranges highlighted in shades of beige which are enumerated by circled numbers.

III. Results

Using the spherical cell model (cf. Fig.1(a)), a method will be presented in the following, with which it is possible to separate the influence of the dispersive material properties of the cell components (e.g. the cytoplasm) from the influence of the geometric/structural composition of the cell on microdosimetric measures (e.g. the transmembrane potential, power density) and effective material properties. One of the central questions to be clarified in this context is whether the cell membrane must also be considered in the modeling at such frequencies or whether it may be neglected since its capacitive nature causes it to be bypassed at high frequencies. This will be discussed in the context of a parameter analysis that varies the diameter of the nucleus so that its share of the cell volume, c_{N}, covers 0.3 to 0.9.

Subsequently, based on the ellipsoidal cell models (cf. Fig.1(b) and (c)), the influence of those organelles enclosed within a membrane on current and power distribution within the cell will be investigated. Here, the comparison of the cell model with and without an ER is the focus of the investigation.

A. Spherical Cell Models

Microdosimetric Investigations of the Spherical Cell Models

In Fig.4(a), the transmembrane potential (TMP) can be observed. The blue curves correspond to the plasma membrane (PM) and the red curves correspond to the nuclear envelope (NE). These

voltages are monitored at the top position of the cell and the nucleus (cf. Fig.2(a)). In general, the TMP of the PM shows a low-pass behavior and that of the NE a bandpass behavior. As introduced earlier, the frequency ranges corresponding to changes in the underlying material properties are plotted at the upper edge of each graph and help to assign observed effects either to changes in the material parameters or to effects caused by the geometrical composition of the electrical «cell system» (cf. Fig.2(d)).

In addition, the size variation of the nucleus shows two effects on the TMP. The larger the nuclear radius, the earlier the PM transitions to low-pass behavior. Correspondingly, band-pass behavior also shifts to lower frequencies while also demonstrating higher TMPs. The range of observed TMPs corresponding to the c_{N} values under investigation is confined by the dotted (i.e., $c_{\mathrm{cell}} = 0.3$) and dashed (i.e., $c_{\mathrm{cell}} = 0.9$) lines and highlighted by the gray-shaded areas in between.

The initial change in the response of the TMP for the nuclear envelope and the PM occurs in MR 1 and thus, is not caused by any change in the underlying material parameters. The shift of the onset of the observed effects can be explained by the geometrical composition of the cell model. Considering the equivalent circuit of the cell in Fig.2(d), two parallel paths exist within the cell, one leading through the nucleus and one bypassing it. In the case of a larger nucleus, the cross-sectional area of the bypassing CP path is reduced resulting in lower conductance. This, in turn, leads to a higher impedance of the whole cell interior (i.e. cytoplasm and nucleus path) causing the accumulation of a significant TMP at the nucleus at lower frequencies. At frequencies larger than 5 MHz in MR 2, the conductivity of the membrane increases and reduces the difference between the impedances of the circuit passing through the nucleus and the one bypassing it. As a result, the TMPs of the different model variants begin to align and seem to converge to a single curve again.

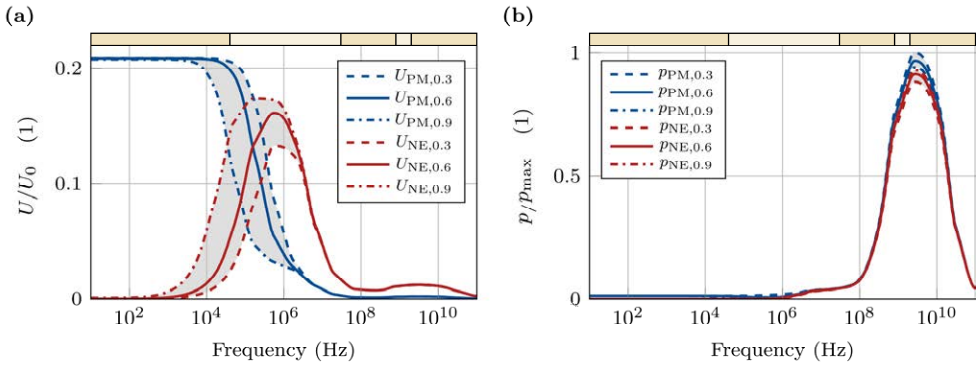

Fig.4: (a) Overview of the transmembrane potential (TMP) normalized to the voltage applied to the computational domain, and (b) the power density normalized to the maximum observed power density. The blue curves show these measures at the plasma membrane (PM), the red ones at the nuclear envelope (NE). The dashed, solid, and dashed-dotted lines show the results of cell models with a volume fraction of the nucleus in the cell of $c_{\mathrm{N}} = 0.3$, $c_{\mathrm{N}} = 0.6$, and $c_{\mathrm{N}} = 0.9$, respectively.

The loss densities corresponding to the TMP can be calculated using $p_i = {U_i}/{t_i}$, where the index i denotes the PM or the NE. The loss density normalized to maximum at the monitored points across the investigated frequency range is displayed in Fig.4(b). For frequencies lower than 1 MHz, the loss density is relatively low compared to that at larger frequencies. This can be explained by the low conductivity of the membrane resulting in a barrier for every current penetrating it. For larger frequencies, the loss densities in both the PM and the NE increase strongly, reaching a global maximum between 1 GHz and 10 GHz. This increase is initiated due to the decreasing relative permittivity of the PM and that of the NE in MR 3. The rapid decrease of the loss density after reaching the maximum is initiated by the decrease of the permittivity of the cytoplasm and the nucleoplasm in MR 5.

Effective Material Parameters of the Spherical Cell Models

The effective material parameters of the simulated cell and its environment are recorded in Fig.5(a) and (b). The effective permittivity clearly displays a range of values between $10\ \mathrm{kHz}$ and $1\ \mathrm{MHz}$ for the various models under investigation. It can be seen that the cell model with the larger nucleus leads to a reduced ability to accumulate charge carriers, due to the previously discussed shift of the transmembrane potential within the cell, especially at the PM. The size of the nucleus thus leads to a lowering of the characteristic frequency of the interfacial polarization. Due to the high conductivity of the EC, no variations within the effective conductivity of the suspension can be observed.

The cell models investigated were compared to analytical models based on mixing rules. The comparison showed maximum relative errors of $<0.5\,\%$ for both conductivity and permittivity over the entire interval. The calculation rules for verification can be found in the Appendix.

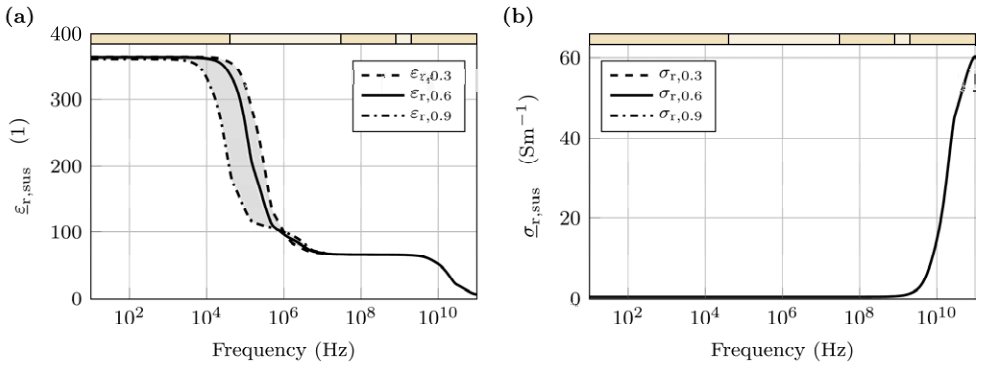

Fig.5: Overview of the effective macroscopic material properties: (a) Effective relative permittivity and (b) effective conductivity for volume fractions of the nucleus in the cell of $c_{\mathrm{N}} = 0.3$, $c_{\mathrm{N}} = 0.6$, and $c_{\mathrm{N}} = 0.9$, respectively.

B. Ellipsoidal Cell Models

Microdosimetric Investigations of the Ellipsoidal Cell Model with an Endoplasmic Reticulum

In order to investigate the influence of organelles enclosed by a membrane, the field distribution within the cell in both ellipsoidal models is studied (cf. Fig.1(b) and (c)). An integral part of this investigation is the comparison between the model with organelles and the one without. Before that, however, the current and loss density distribution within the cell with organelles is analyzed and displayed in Fig.6.

As an illustrative example, Fig.6(a) shows the distribution of the current density, $|\underline{J}|$, and the power density, *p,* in the XY plane (cf. Fig.1(i)) at different frequencies. According to the color scale on the right, red areas indicate maximum values and light areas indicate minimum values. Considering $|\underline{J}|$ or p as a function of space, $\vec{r}$ and frequency f,

$$J_{\min/\max}(f) = \begin{cases} \min\limits_{\vec{r}} |\underline{\vec{J}}(f,\vec{r})| \\ \max\limits_{\vec{r}} |\underline{\vec{J}}(f,\vec{r})| \end{cases} \tag{10}$$

$$p_{\min/\max}(f) = \begin{cases} \min\limits_{\vec{r}} p(f,\vec{r}) \\ \max\limits_{\vec{r}} p(f,\vec{r}) \end{cases} \tag{11}$$

can be used to relate the minimum and maximum values at the individual frequency points and compare them quantitatively. For better visualization, these minimum and maximum values are normalized to the global maxima observed in the frequency range under investigation, as formulated here:

$$J_{\mathrm{abs,max}} = \max_f J_{\mathrm{max}}(f) \tag{12}$$

$$p_{\mathrm{abs,max}} = \max_f p_{\mathrm{max}}(f) \tag{13}$$

Fig.6(b) and (c) display the normalized amplitude ratio,

$$J_{\mathrm{n,min/max}}(f) = 20\ \log_{10}\left({J_{\mathrm{min/max}}(f)}/{J_{\mathrm{abs,max}}}\right) \tag{14}$$

$$p_{\mathrm{n,min/max}}(f) = 10\ \log_{10}\left({p_{\mathrm{min/max}}(f)}/{p_{\mathrm{abs,max}}}\right) \tag{15}$$

The spectral responses indexed by *y* correspond to the field plots in Fig.6(a). In this figure, it can be seen that the cisternal organelle structures, which are concentrated around the nucleus, ensure that the field densities in the cytoplasm are heterogeneously distributed. The layered structure of the membranes of the ER around the nucleus throughout the CP means that the current entering the cell is primarily conducted via the outer cell edge and the current and loss densities around and in the nucleus are comparatively low, especially at low frequencies. At a frequency of $10\,\mathrm{Hz}$ for example, it can be seen that almost no current flows or losses occur in the ER or the nucleus. However, these compartments both become increasingly penetrable as the frequency increases. At frequencies of $10\,\mathrm{MHz}$ and above, a current distribution is established within the cell that corresponds approximately to the area of the respective compartments on the (cross-) sectional plane of the cell.

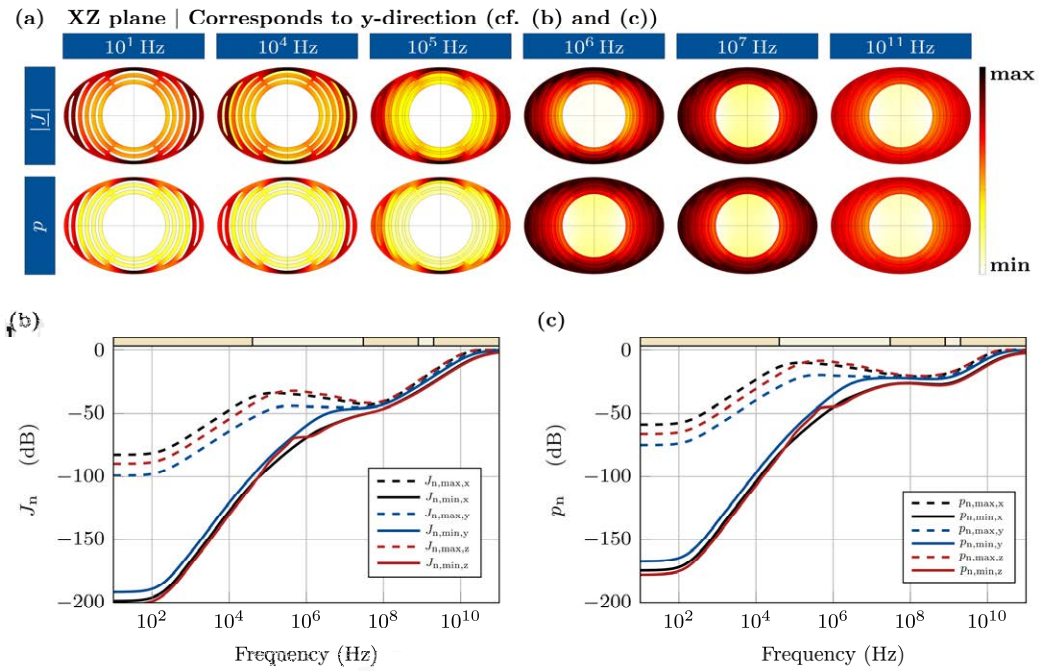

Fig.6: (a) The current density, $|\underline{J}|$, and the loss distribution, p, are displayed in the XZ plane at different frequencies. Maximum values are indicated by red areas and minimum values by light areas. The field plots can be observed while applying a voltage in the y-direction. (b)-(c). Quantitative assessment of the minimum and maximum values of both J_n (cf. Eq. (14)) and the p_n (cf. Eq. (15)) plotted on a logarithmic scale.

In Fig.6(b), it can be observed that the maximum current density at $10\,\mathrm{Hz}$ is about $100\,\mathrm{dB}$ smaller than at $100\,\mathrm{GHz}$. The reason for this is the high conductivity of the extracellular medium and the low conductivity of the plasma membrane. Roughly speaking, the current density within the cell increases strongly between $100\,\mathrm{Hz}$ and $1\,\mathrm{MHz}$. Furthermore, the difference between the minimum

and maximum current density decreases from about $90\,\mathrm{dB}$ to $< 1.5\,\mathrm{dB}$. For frequencies larger than $1\,\mathrm{MHz}$, the current density increases further and reaches a plateau around $100\,\mathrm{GHz}$. To summarize, it can be noted that low cell currents with high relative current density differences occur at frequencies $< 1\,\mathrm{MHz}$ while high currents with lower differences are observed at frequencies $> 1\,\mathrm{MHz}$. These statements can also be made for the loss density shown in Fig.6(c).

Tab. 4 provides an overview over the normalized minimum and maximum current and loss densities in the frequency interval between $1\,\mathrm{GHz}$ and $100\,\mathrm{GHz}$. It is worth noting that the ratio between the minimum and maximum current density is between 1.016 and 1.157 and that of the loss density between 1.043 and 1.342, and thus, a non-negligible difference between currents and losses in the outer edge of the cell interior and the nucleus exists.

Tab. 4: Overview of the normalized minimum and maximum current and loss densities in the frequency interval between 1 GHz and 100 GHz.

Current Density				
Frequency (GHz)	$J_{\mathrm{n,min,y}}$	$J_{\mathrm{n,max,y}}$	$J_{\mathrm{n,min,y}} - J_{\mathrm{n,max,y}}$	$J_{\mathrm{min}}/J_{\mathrm{max}}$
100	-0.182	-0	-0.182	1.016
50	-1.012	-0.87	-0.142	1.021
10	-7.908	-6.74	-1.168	1.144
1	-26.9	-25.63	-1.27	1.157
Loss Density				
Frequency (GHz)	$p_{\mathrm{n,min,y}}$	$p_{\mathrm{n,max,y}}$	$p_{\mathrm{n,min,y}} - p_{\mathrm{n,max,y}}$	$p_{\mathrm{min}}/p_{\mathrm{max}}$
100	-0.182	-0	-0.182	1.043
50	-0.679	-0.364	-0.315	1.075
10	-7.15	-5.987	-1.163	1.307
1	-21.897	-20.618	-1.279	1.342

To provide a comprehensive analysis, Fig.7(a) and (c) display the spectral response of the relative current and loss distribution within the cell with an ER. These quantities are defined as

$$\frac{I_i}{I_{\mathrm{cell}}} \quad \text{and} \quad \frac{P_i}{P_{\mathrm{cell}}} \tag{16}$$

where $i \in \{\mathrm{CP};\ \mathrm{NP};\ \mathrm{ER}\}$ denotes the cytoplasm, nucleoplasm or endoplasmic reticulum. The currents

$$I_i(f) = \iint \vec{J}(\vec{r}, f) \cdot \vec{n}\, dA_i \tag{17}$$

and losses

$$P_i(f) = \iiint p(\vec{r}, f) dV_i \tag{18}$$

are derived by integrating the current densities in the (cross-) sectional planes and the loss densities in the compartments (cf. Fig.1(d)-(f) and (j)-(k)) respectively. The cell currents and cell losses are defined as

$$I_{\mathrm{cell}}(f) = I_{\mathrm{CP}}(f) + I_{\mathrm{NP}}(f) + I_{\mathrm{ER}}(f) \tag{19}$$

$$P_{\mathrm{cell}}(f) = P_{\mathrm{CP}}(f) + P_{\mathrm{NP}}(f) + P_{\mathrm{ER}}(f) \tag{20}$$

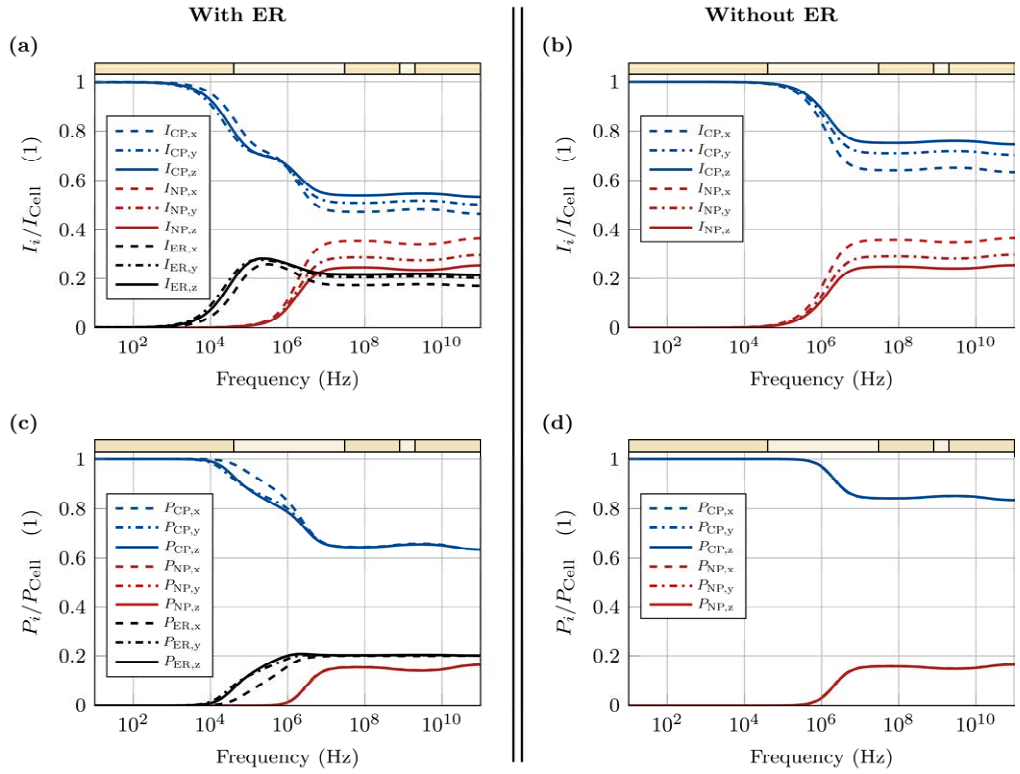

Fig.7: Comparison of the spectral response of the current and loss distribution within the individual cell compartments between the cell model with an endoplasmic reticulum and the one without. The indices, CP, NP and ER, denote the cytoplasm, nucleoplasm and endoplasmic reticulum.

Here it can be clearly seen that cell currents at frequencies $< 1\,\mathrm{kHz}$ are almost exclusively conducted in the cytoplasm. At frequencies $> 1\,\mathrm{kHz}$, the cell current also flows through the cisternae of the ER. Furthermore, it can be seen that the nucleus only conducts a part of the cell current from a frequency $> 100\,\mathrm{kHz}$ upwards. At frequencies of $10\,\mathrm{MHz}$ and higher, a current distribution is established within the cell that corresponds approximately to the area of the respective compartments on the (cross-)sectional plane of the cell. Due to the different dimensions of the individual compartments in the (cross-)sectional plane, a slightly anisotropic current distribution can be observed. These observations can also be transferred to the relative cell losses. Another finding is that the nucleus conducts current at higher frequencies than the rest of the organelles, because of the thicker membrane assumed in the model ($t_M = 7\,\mathrm{nm}$ and $t_{\mathrm{NE}} = 40\,\mathrm{nm}$). In addition, Fig.7(b) and (d) display the relative current and loss distributions for the model without an endoplasmic reticulum to better relate them to those of the model with an endoplasmic reticulum.

Comparison of the Ellipsoidal Cell Models with and without an Endoplasmic Reticulum

In the following, the field distributions of the cell model with an ER (see Fig. 1(c)) are compared with those of the model without ER (see Fig.1(b)). Fig.8(a) displays the spatial differences of the current density ΔJ, and the loss density, Δp, at different frequency point in the XZ plane, where these are defined as follows:

$$\Delta J(f,\vec{r}) = \frac{|\underline{\vec{J}}(f,\vec{r})|_{\mathrm{ER}} - |\underline{\vec{J}}(f,\vec{r})|_{\mathrm{EC}}}{\left\langle |\underline{\vec{J}}(f,\vec{r})| \right\rangle_{\mathrm{ER}}} \tag{21}$$

$$\Delta p(f,\vec{r}) = \frac{p(f,\vec{r})_{\mathrm{ER}} - p(f,\vec{r})_{\mathrm{EC}}}{\langle p(f,\vec{r}) \rangle_{\mathrm{ER}}} \tag{22}$$

The indices ER and EC denote the endoplasmic reticulum and the ellipsoidal cell respectively. $\left\langle|\vec{J}(f,\vec{r})|\right\rangle_{\mathrm{ER}}$ and $\langle p(f,\vec{r})\rangle_{\mathrm{ER}}$ are the spatial averages within the whole cell. Thus, these quantities represent the maximum and minimum spatial differences within the cell normalized to the spatial average at a specific frequency. Applying Eq. (10) to (11) to ΔJ and Δp, the minimum and maximum spatial differences of both the current and loss density can be determined and are defined as

$$\Delta J_{\mathrm{min/max}}(f) = \begin{cases} \min\limits_{\vec{r}} \Delta\vec{J}(f,\vec{r}) \\ \max\limits_{\vec{r}} \Delta\vec{J}(f,\vec{r}) \end{cases} \tag{23}$$

$$\Delta p_{\mathrm{min/max}}(f) = \begin{cases} \min\limits_{\vec{r}} \Delta p(f,\vec{r}) \\ \max\limits_{\vec{r}} \Delta p(f,\vec{r}) \end{cases} \tag{24}$$

To interrelate and quantitatively assess the field plots in Fig.8(a), $\Delta J_{\mathrm{min/max}}(f)$ and $\Delta p_{\mathrm{min/max}}(f)$ are displayed in Fig.8(b) and (c) respectively.

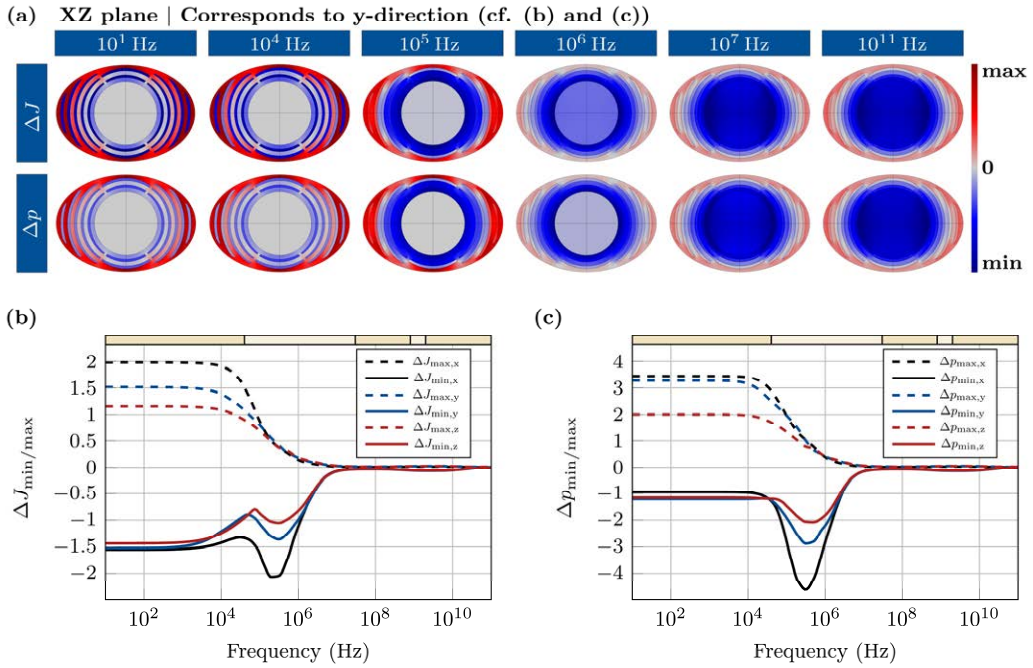

Fig.8: (a) The distribution of current density, ΔJ, and the power density, Δp, displayed in the XZ plane at different frequencies. ΔJ and Δp are defined as formulated in Eq. (21) and (22). Maximum values are indicated by red areas and minimum values by light areas. The field plots can be observed while applying a voltage in the y-direction. (b)-(c) Quantitative assessment of the minimum and maximum values of both ΔJ (cf. eq. (23)) and Δp (cf. eq. (24)) are plotted.

According to the numerator term in equations (21) and (22), the red (positive) and blue (negative) areas in Fig.8(a) can be interpreted as follows. In the red areas, the ER model has field strengths that are higher than those of the EC model, and in the blue areas, the EC model has field strengths that are higher than those of the ER model. This graphical evaluation shows in which areas the field magnitudes are overestimated or underestimated in a model *without* organelles. Grey regions indicate areas where there are no, or only very small, differences between the models with and without an ER. Looking at ΔJ and Δp at low frequencies ($\leq 10\,\mathrm{kHz}$), it can be seen that an ER enclosed by a membrane has a large influence on the current and loss density, as these regions are electrically shielded. At frequencies larger than $10\,\mathrm{kHz}$ and less than $10\,\mathrm{MHz}$, it becomes very clear that although shielding provided by the ER is not absolute, the current distribution is changed in such

a way that currents are mainly conducted at the outer edge of the cell compared to the model without ER. In particular, the field images at $1\ \mathrm{MHz}$ show that the cascade-like concentric layering of the ER around the nucleus leads to its electrical shielding, thus, the EC model overestimates the current flowing through or around the nucleus. Looking at the spectral responses of the minimum and maximum values of ΔJ and Δp illustrated in Fig.8(a) and (b), it can be seen that the current and loss densities for frequencies $> 10\ \mathrm{MHz}$ are relatively homogeneous in the entire cell space.

Effective Material Parameters of the Ellipsoidal Cell Models

The effective material parameters of the simulated suspension are displayed in Fig.9(a) and (c) for the cell model with an endoplasmic reticulum and in Fig. (b) and (d) for the model without an ER. The indices, x, y and z, denote the direction of the voltage applied in the capacitor experiment, based on the semi-axes of the cell defined in these directions. Therefore, index x means that the voltage is applied in the x-direction and thus aligned with the semi-axis in the x-direction. Comparing the effective macroscopic permittivity of both models, $\varepsilon_{\mathrm{r,sus}}$, it can be observed that there is no difference in the static permittivity for frequencies < 10 kHz. The direction of the applied voltage, however, leads to different values for the permittivity while the pattern of this anisotropy remains the same between the two models. In the frequency range highlighted in grey (i.e. between 10 kHz and 1 MHz), differences between the models can be observed. In the model with an ER, the characteristic frequency of the interfacial polarization process shifts towards lower frequencies, so that the observed Maxwell-Wagner roll-off starts at low frequencies. This is especially true when the voltage is applied in the x-direction, since in this case, the largest number of cisternae lies between the PM and the NE (cf. Fig. 1(c)). This can be attributed to the changes in the transmembrane potential as discussed in earlier (see Sec. III A). At frequencies where the impedance of the PM loses its overriding dominance, the concentric arrangement of many cisternal membranes leads to a series of internal voltage drops and a potential distribution that is oriented toward the interior of the cell. For frequencies > 1 MHz, all curves merge at the same value and show the same trends in both models.

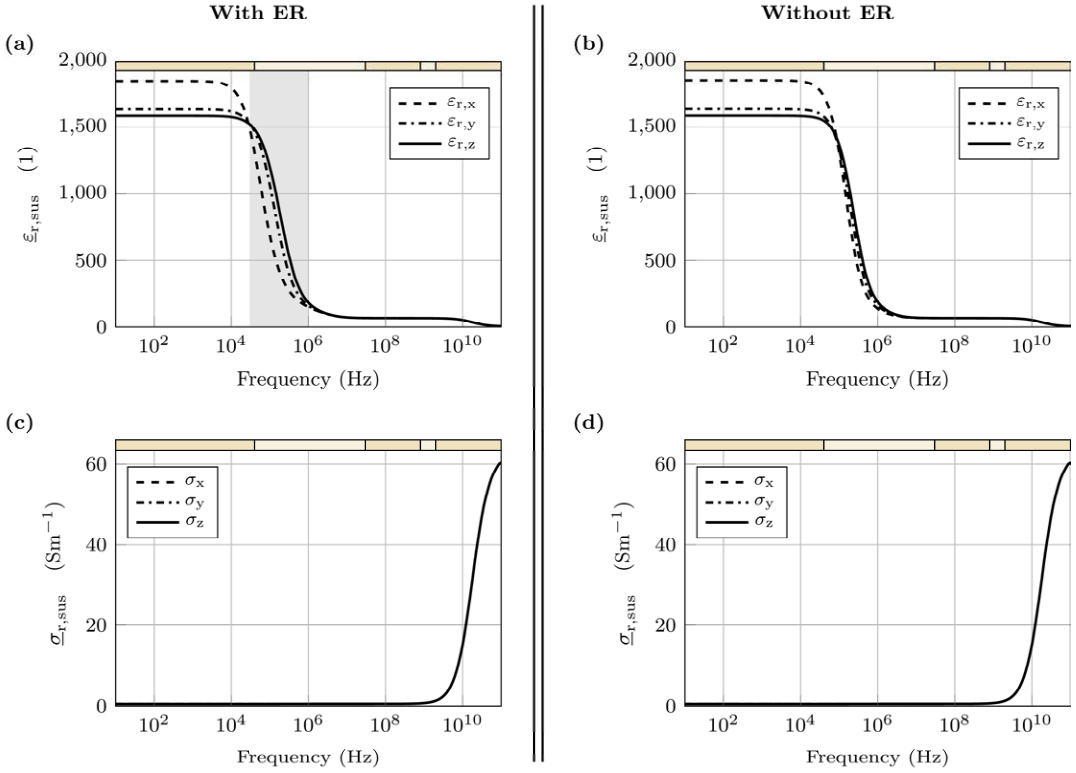

Fig.9: Overview of the effective material properties of the ellipsoidal cell models: (a) and (c) display the effective permittivity, $\varepsilon_{\mathrm{r,sus}}$, and conductivity, σ_{sus}, of the cell suspension with cells including an endoplasmic reticulum (ER), and (b) and (d) display the values of a suspension without an endoplasmic reticulum. The indices in the legend, x, y and z, denote for the direction of the voltage applied in the capacitor experiment.

Due to the extremely high conductivity of the extracellular medium, the ER has no impact on the effective conductivity of the suspension. As already observed for the spherical cell model, the effective conductivity of the ellipsoidal model is primarily governed by the material properties of the extracellular space.

IV. Conclusion and Outlook

Using the method presented, the influence of the cell structure/geometry can be separated from that of the dispersive material properties, with each of these influences having a direct effect on both microdosimetric measures and on macrosopic effective material parameters. For the spherical cell model, it has been shown that the cell membrane has to be considered at low frequencies ($< 1\,\mathrm{MHz}$) as well as at high frequencies ($> 1\,\mathrm{MHz}$) for the following reasons. At low frequencies, the modeling of the membrane is necessary because, in the absence of induced physiological changes such as electroporation, the membrane electrically shields the interior of the cell and has a high impact on the effective relative permittivity of the cell system. At high frequencies, modeling of the membrane is necessary because the different characteristic frequencies of the dispersive material functions lead to peaks in the power dissipation density in the membrane, which must be considered in the context of microdosimetric investigations.

The microdosimetric investigation of the ellipsoidal cell model involving the ER showed that a system of organelles enclosed by membranes has a large influence on the field distribution within the cell. Thus, it has been shown that organelle structures may act like barriers at low frequencies ($f < 10\,\mathrm{kHz}$) due to their material properties. As a result, cell currents tend to be conducted across the outer edge of the cell. In general, the maximum relative difference between the largest and smallest local current and loss densities occurs at such low frequencies, with the high resistance of the cell membrane allowing only small currents to enter the cell. In this context, however, it should be noted that not all applications require a background fluid as conductive as that assumed in our simulations, and thus higher currents could enter the cell.

At frequencies between $10\,\mathrm{kHz}$ and $10\,\mathrm{MHz}$ the membranes become increasingly penetrable, causing the cell current to increase and the relative differences between minimum and maximum field strengths to decrease, resulting in the field distribution becoming increasingly homogeneous. Despite this trend toward a more homogeneous current and power distribution, it should be noted that the ratio between the maximum and the minimum current density is still 1.157 and that for the power density is still 1.342 at frequencies as high as $1\,\mathrm{GHz}$ and should not be considered to be negligible. In particular, directly comparing the cell models with and without an ER, it can be shown that the cisternae of the organelles strongly influence the current distribution despite the better conductivity of the membrane for higher frequencies. Although these no longer act as rigid barriers, they increase the resistance of the current path that leads across the nucleus by layering many membranes on top of each other, as a result of which the current density in the nucleus is significantly higher in the model without an ER. This can also be observed for frequencies $> 10\,\mathrm{MHz}$, and thus also has consequences frequencies implemented in 5G telecommunication standards (i.e. 600 MHz to 6 GHz and 24 GHz to 54 GHz). Microdosimetric studies evaluating potential health risks at the cellular level should therefore include cell organelles in the modeling.

Outlook

Using generic cell and organelle morphology, it has already been shown here that organelles such as the ER have a major influence on the internal current and power distribution within a cell across the whole investigated frequency range. However, due to the generic modeling approach, the results of these studies can only be qualitatively applied to real cells. Therefore, to obtain more quantitative results, a useful next step would be to develop cell models that take into account the asymmetric, stochastic nature of real eukaryotic cells by first capturing the internal structure of as large a number as possible and transferring them to computer models. However, transferring realistic cell morphologies into simulation models is per se a major challenge, since, for example, the dimensions of organelle cisternae in reality are much smaller and the density of membrane layers much larger than in the cell models presented here. Another future step would be to simulate multicellular structures to determine the effects of different model details (e.g., the density of the ER) on the

effective material properties of tissues in the context of multiscale modeling as developed in [Froehlich et al, 2014]. This would allow the determination of the EM energy intake at the microstructural level in cells and their organelles as part of a realistic exposure scenario.

Acknowledgments

This work was funded by the Swiss Research Foundation for Electricity and Mobile Communications (FSM) at ETH Zürich in the framework of FSM-Project No. A2019-01. We also acknowledge the partial support from the Deutsche Forschungsgemeinschaft (DFG, German Research Foundation) under Project 287022738 of the CRC/TRR 196 MARIE in the context of project M03 and the partial funding by the project "Konzepte für Ende-zu-Ende Terahertz 6G-Mobilfunk" (no. 16KISKK039) in the framework of the BMBF (German Federal Ministry of Education and Research) joint research project 6GEM.

Appendix

In order to validate the computational model used to determine the effective material properties of the cell and cell suspension, the simulations considering the simple spherical cell model are compared with analytical mixing rules. As described in [Asami, 1989] and [Feldman, 2003], the effective permittivity of the cell $\underline{\varepsilon}_{\mathrm{cell}}$ is modelled as double-layered shell

$$\underline{\varepsilon}_{\mathrm{cell}} = \underline{\varepsilon}_{\mathrm{PM}} \frac{2\,(1-v_1)+(1+2v_1)E_1}{(2+v_1)+(1-v_1)E_1} \tag{25}$$

where the geometrical parameter v_1 represents for the volume ratio between the plasma membrane and the inner layers and the intermediate parameter E_1 the effective permittivity of the lower layers weighted by the permittivity of the upper layer, which is in this case the plasma membrane. The parameters v_1 and E_1 is given by

$$v_1 = \left(1 - \frac{t_{\mathrm{M}}}{r_{\mathrm{cell}}}\right)^3 \tag{26}$$

$$E_1 = \frac{\underline{\varepsilon}_{\mathrm{CP}}}{\underline{\varepsilon}_{\mathrm{PM}}} \cdot \frac{2\,(1-v_2)+(1+2\,v_2)\,E_2}{(2+v_2)+(1-v_2)\,E_2} \tag{27}$$

Similar to the calculation of the effective permittivity of the whole cell, the intermediate parameter E_1 itself is also calculated from the intermediate parameters v_2 and E_2. These can be calculated according to

$$v_2 = \left(\frac{r_{\mathrm{N}}}{r_{\mathrm{cell}}-t_{\mathrm{M}}}\right)^3 \tag{28}$$

$$E_2 = \frac{\underline{\varepsilon}_{\mathrm{NP}}}{\underline{\varepsilon}_{\mathrm{CP}}} \cdot \frac{2\,(1-v_3)+(1+2\,v_3)\,E_3}{(2+v_3)+(1-v_3)\,E_3} \tag{29}$$

The concatenation of intermediate parameters ends with the inner layer consisting of the nucleus and its envelope.

$$v_3 = \left(1 - \frac{t_{\mathrm{NE}}}{r_{\mathrm{N}}}\right)^3 \tag{30}$$

$$E_3 = \frac{\underline{\varepsilon}_{\mathrm{NP}}}{\underline{\varepsilon}_{\mathrm{NE}}} \tag{31}$$

After calculating the effective dielectric constant of the cell according to the above algorithm, the effective material parameters of the mixture are calculated based on the Hanai-Bruggeman equation as presented in [Asami, 2002]

$$0 = \frac{\underline{\varepsilon}_{\mathrm{mix}} - \underline{\varepsilon}_{\mathrm{cell}}}{\underline{\varepsilon}_{\mathrm{EC}} - \underline{\varepsilon}_{\mathrm{cell}}} \cdot \sqrt[3]{\frac{\underline{\varepsilon}_{\mathrm{EC}}}{\underline{\varepsilon}_{\mathrm{mix}}}} - (1 - c_{\mathrm{cell}}) \qquad (32).$$

References

Asami K, Hanai T, Koizumi N. 1979. Dielectric properties of yeast cells. J Membrane Biol 28(2-3): 169-180, doi: 10.1007/BF01869695

Asami K, Takahashi Y, Takashima S. 1989. Dielectric properties of mouse lymphocytes and erythrocytes. BBA Mol Cell Res 1010(1):49-55. doi: 10.1016/0167-4889(89)90183-3

Asami K. 2002. Characterization of heterogeneous systems by dielectric spectroscopy. Prog Poly Scie 27(8): 1617-1659. doi: 10.1016/S0079-6700(02)00015-1

Chien JC, Ameri A, Yeh EC, Killilea AN, Anwar M, Niknejad AM. 2018. A high-throughput flow cytometry-on-a-CMOS platform for single-cell dielectric spectroscopy at microwave frequencies. Lab on a Chip 18(14). doi: 10.1039/c8lc00299a

COMSOL AB [Internet]. COMSOL Multiphysics (V. 5.6) [2021 Sep 22]. Available from: http://www.comsol.com

de Angelis A, Denzi A, Merla C, Andre FM, Garcia-Sanchez T, Mir LM, Apollonio F, Liberti M. 2019. A microdosimetric realistic model to study frequency-dependent electroporation in a cell with endoplasmic reticulum. 2019 49th European Microwave Conference (EuM C2019). 212-215. doi: 10.23919/EuMC.2019.8910909

de Angelis A, Denzi A, Merla C, Andre FM, Mir LM, Apollonio F, Liberti M. 2020. Confocal microscopy improves 3D microdosimetry applied to nanoporation experiments targeting endoplasmic reticulum. Front Bioeng Biotec 8: 1079. doi: 10.3389/fbioe.2020.552261

Denzi A, Merla C, Camilleri P, Paffi A, d'Inzeo G, Apollonio F, Liberti M. 2013. Microdosimetric study for nanosecond pulsed electric fields on a cell circuit model with nucleus. J Membrane Biol 256(10): 761-767. doi: 10.1007/s00232-013-9546-7

Denzi A, Merla C, Palego C, Paffi A, Ning Y, Multari CR, Cheng X, Apollonio F, Hwang JCM, Liberti M. 2015. Assessment of cytoplasm conductivity by nanosecond pulsed electric fields. IEEE Trans Bio-Med Eng 62(6): 1595-1603. doi: 10.1109/TBME.2015.2399250

Denzi A, Escobar JAA, Nasta C, Merla C, Benassi C, Consales C, Apollonio F, Liberti M. 2016. A microdosimetry study for a realistic shaped nucleus. 2016 38th Annual International Conference of the IEEE Engineering in Medicine and Biology Society (EMBC). 4189-4192. doi: 10.1109/EMBC.2016.7591650

Denzi A, Hanna H, Andre FM, Mir LM, Apollonio F, Liberti M. 2017. Microdosimetry for pulsed E fields in a realistic models of cells and endoplasmic reticulum. 2017 14th International Conference on Synthesis, Modeling, Analysis and Simulation Methods and Applications to Circuit Design (SMACD). 1-3. doi: 10.1109/SMACD.2017.7981606.

Denzi A, Merla C, Andre FM, Garcia-Sanchez T, Mir LM, Apollonio F, Liberti M. 2018. Shared knowledge, gaps and challenges of microdosimetry: Realistic models of cells and endoplasmic reticulum. 2018 IEEE International Microwave Biomedical Conference (IMBioC). 19-21. doi: 10.1109/IMBIOC.2018.8428949

Ermolina I, Polevaya Y, Feldman Y. 2000. Analysis of dielectric spectra of eukaryotic cells by computer modeling. Euro Biohphys J 29(2): 141-145. doi: 10.1007/s002490050259

Ermolina I, Polevaya Y, Feldman Y, Ginzburg BZ, Schlesinger M. 2001. Study of normal and malignant white blood cells by time domain dielectric spectroscopy. IEEE Trans Dielect Electr Insul 8(2): 253-261. doi: 10.1109/94.919948

Feldman Y, Ermolina I, Hayashi Y. 2003. Time domain dielectric spectroscopy study of biological systems. IEEE Trans Dielect Electr Insul 10(5): 728-753. doi: 10.1109/TDEI.2003.1237324

Feng Y, Huang L, Zhao P, Liang F, Wang W. 2019. A microfluidic device integrating impedance flow cytometry and electric impedance spectroscopy for high-efficiency single-cell electrical property measurement. Anal Chem 91(23): 15204-15212. doi: 10.1021/acs.analchem.9b04083

Froehlich J, Huclova S, Beyer C, Erni D. 2014. Computational Biophysics of the Skin. book chapter 12, Accurate multi-scale skin model suitable for determining sensitivity and specificity of changes of skin components. 353-394, Singapore: Pan Stanford Publishing Pte. Ltd. Isbn: 978-981-4463-84-3

García-Sánchez T, Merla C, Fontaine J, Muscat A, Mir LM. 2018. Sine wave electropermeabilization reveals the frequency-dependent response of the biological membranes. BBA Biomembranes 1860(5): 1022-1034. doi: 10.1016/j.bbamem.2018.01.018

Gowrishankar TR, Esser AT, Vasilkoski Z, Smith KC, Weaver JC. 2006. Microdosimetry for conventional and supra-electroporation in cells with organelles. Biochem Biophys Res Com 341(4): 1266-1276. doi: 10.1016/j.bbrc.2006.01.094

Gowrishankar TR, Weaver JC. 2006. Electrical behavior and pore accumulation in a multicellular model for conventional and supra-electroporation. Biochem Biophys Res Com 349(2): 643-653. doi: 10.1016/j.bbrc.2006.08.097

Guo Y, Yagi I, Uchida S, Tochikubo F, Takano M, Wakizaka Y, Enjoji T. 2021. Basic study of dielectric properties of cancer cells by dielectrophoretic velocimetry. Electron Comm Jpn 104(2). doi: 10.1002/ecj.12318

Huclova S, Erni D, Froehlich J. 2010. Modeling effective dielectric properties of materials containing diverse types of biological cells. J Appl Phys D 43(36): 365405. doi: 10.1088/0022-3727/43/36/365405

Huclova S. 2011. Modeling of cell suspensions and biological tissue for computational electromagnetics. Diss. ETH Zürich, No. 19863, Zürich.

[ICNIRP] Int. Comm. on Non-Ionizing Radiation Protection. 2020. ICNIRP Guidelines for Limiting Exposure to Electromagnetic Fields (100 KHz-300 GHz). Health Phys. 118(5): 483-524. doi: 10.1097/HP.0000000000001210

[IEEE] Institute of Electrical and Electronics Engineers. 2019. IEEE Std C95.1-2019 - IEEE standard for safety levels with respect to human exposure to electric, magnetic, and electromagnetic fields, 0 Hz to 300 GHz. doi: 10.1109/IEEESTD.2019.8859679

Jerbic K, Neumann K, Svejda JT, Sievert B, Rennings A, Erni D. 2020. Limits of effective material properties in the context of an electromagnetic tissue mModel. IEEE Access 8: 223806-223826: doi: 10.1109/ACCESS.2020.3045327

Kitano H. 2002. Computational systems biology. Nature 420(6912): 206-210. doi: 10.1038/nature01254

Krakovsky I, Myroshnychenko V. 2002. Modeling dielectric properties of composites by finite-element method. J Appl Phys 92(11): 6743-6748. doi: 10.1063/1.1516837

Kotnik T, Miklavčič D. 2000. Theoretical evaluation of the distributed power dissipation in biological cells exposed to electric fields. Bioelectromagnetics 21(5): 385-394. doi: 10.1002/1521-186X(200007)21:5<385::AID-BEM7>3.0.CO;2-F

Lisin R, Ginzburg BZ, Schlesinger M, Feldman Y. 1996. Time domain dielectric spectroscopy study of human cells. I. Erythrocytes and ghosts. BBA Biomembranes 1280(1): 34-40. doi: 10.1016/0005-2736(95)00266-9

The MathWorks Inc [Internet]. MATLAB (R 2020b) [2021 Sep 22]. Available from: http://wwwmathworks.com

Merla C, Liberti M, Marracino P, Muscat A, Azan A, Apollonio F, Mir LM. 2018. A wide-band bio-chip for realtime optical detection of bioelectromagnetic interactions with cells. Sci Rep 8(1): 5044. doi: 10.1038/s41598-018-23301-w

Merla C, Liberti M, Consales C, Denzi A, Apollonio F, Marino C, Benassi B. 2019. Evidences of plasma membrane-mediated ROS generation upon ELF exposure in neuroblastoma cells supported by a computational multiscale approach. BBA Biomembranes 1861(8): 1446-1457. doi: 10.1016/j.bbamem.2019.06.005

Merla C, Liberti M, Apollonio F, d'Inzeo G. 2009. Quantitative assessment of dielectric parameters for membrane lipid bi-layers from RF permittivity measurements. Bioelectromagnetics 30(4): 286-298. doi: 10.1002/bem.20476

Merla C, Denzi A, Paffi A, Casciola M, d'Inzeo G, Apollonio F, Liberti M. 2012. Novel passive element circuits for microdosimetry of nanosecond pulsed electric fields. IEEE Trans Bio-Med Eng 59(8): 2302-2311. doi: 10.1109/TBME.2012.2203133

Peyman A, Gabriel C, Grant EH. 2007. Complex permittivity of sodium chloride solutions at microwave frequencies. Bioelectromagnetics 28(4): 264-274. doi: 10.1002/bem.20271

Polevaya Y, Ermolina I, Schlesinger M, Ginzburg BZ, Feldman Y. 1999. Time domain dielectric spectroscopy study of human cells II, Normal and malignant white blood cells. BBA Biomembranes 1419(2):257-271. doi: 10.1016/S0005-2736(99)00072-3

Pucihar G, Kotnik T, Valic B, Miklavčiči D. 2006. Numerical determination of transmembrane voltage induced on irregular shaped cells. Ann Biomed Eng 34(4): 642-652. doi: 10.1007/s10439-005-9076-2

Sihvola A. 2008. Electromagnetic Mixing Formulas and Applications. London (UK): The Institution of Engineering and Technology.

Towhidi L, Kotnik T, Pucihar G, Firoozabadi SMP, Mozdarani H, Miklavčičic D. 2008. Variability of the minimal transmembrane voltage resulting in detectable membrane electroporation. Electromag Biol Med 27(5): 372-385. doi: 10.1080/15368370802394644

Weaver JC. 2003. Electroporation of biological membranes from multicellular to nano scales. IEEE Trans Dielect Electr Insul 10(5): 754-768. doi: 10.1109/TDEI.2003.1237325